Self-Correcting-Guided Generalized Contrastive Learning Framework for Small-Sample PV Fault Diagnosis With Cloud-Edge Collaboration

Qi Liu ⬡, Bo Yang ⬡, *Senior Member, IEEE*, Mingxuan Cai, Yuxiang Liu ⬡,
Kai Ma ⬡, *Senior Member, IEEE*, and Xinping Guan ⬡, *Fellow, IEEE*

***Abstract*—Intelligent fault diagnosis of photovoltaic (PV) arrays in small-sample scenarios remains challenging due to poor model accuracy and generalization. Existing methods fail to simultaneously address issues of varied operation conditions and insufficient samples, leading to the limited applicability of models built by few-shot learning. In addition, factors, such as data transmission and computation costs, also need to be considered. Therefore, this article proposes a cloud-edge collaborative self-correcting-guided generalized contrastive learning framework for small-sample PV fault diagnosis. First, an end-to-end self-correcting model is proposed to eliminate the influence of variable environments. Then, a self-correcting scheme is integrated with contrastive learning to achieve model generalization, and a type screening method is designed to improve model accuracy. Furthermore, a fast fault filtering mechanism is proposed to enhance the algorithm efficiency with cloud-edge collaboration. Both simulation and real data are utilized to validate the proposed method.**

***Index Terms*—Cloud-edge, contrastive learning, few-shot learning, photovoltaic (PV) arrays, self-correcting.**

I. INTRODUCTION

PHOTOVOLTAIC (PV) arrays are essential components in PV systems. Their fault diagnosis is crucial for intelligent operation and maintenance to ensure the security, stability, and profitability of large PV stations. These arrays affect the performance, reliability, and safety of the systems. Owing to the powerful automatic feature extraction capability of neural networks, data-driven methods based on machine learning (ML) have gradually become mainstream.

At the laboratory level, significant progress has been made in ML-based fault diagnosis methods, such as convolutional neural network (CNN) [1], extreme learning machine (ELM) [2], and active learning (AL) [3]. Although some methods have reported even 100% fault diagnosis accuracy, they are typically designed for scenarios with comprehensive datasets, where fault samples are abundant and data quality is superior. These methods fail to be directly deployed in practical applications because it is impractical to collect samples of all fault types under complex and varied operating conditions. The accumulation of fault sample data is a protracted process and is imperative to develop fault diagnosis methods for small-sample scenarios.

In situations when fault samples are limited, some few-shot learning methods have been proposed to reduce the demand for data. Kumar et al. [4] proposed a semi-supervised learning method with autoencoders for reducing the amount of data required for fault classification. Wang et al. [5] constructed a dual graph neural network with residual blocks to achieve fault diagnosis in environments with limited data availability. In addition, transfer learning, meta-learning (MTL), and generative adversarial networks, etc. are also commonly used methods. However, the training sets employed in these methods generally include all fault types targeted for diagnosis and require a certain number of samples for each type. In the initial operation phase of PV systems, fault samples are few and the types are incomplete. This poses significant challenges to the sample expansion of existing methods.

Recently, contrastive learning techniques have been widely used in many fields to conduct classification in the context of limited data, such as social network location recommendation service [6], fault diagnosis of rolling element bearings [7], and graph classification [8]. Since contrastive learning models are trained by similarity comparisons rather than data labels, they can better exploit the feature representations in the case of small samples. In addition, problems including high costs of data transfer and computation, and inefficient algorithm execution also need to be urgently addressed [9]. In the field of fault diagnosis, cloud-edge collaboration is a trending paradigm [10]. The

advantages of real-time processing at the edge and computing capacity in the cloud can be utilized in a complementary manner.

Despite the great progress made by the methods mentioned above, there are still many issues that remain to be resolved. First, there is a lack of effective type-selecting methods to realize economical PV sample expansion for extremely small-sample scenarios. It is costly to collect further samples of all types, but selective collection is an acceptable solution. Second, the prior knowledge derived from the electrical characteristics of the I-V curve is overlooked. Existing methods primarily focus on optimizing data and network architectures, while failing to integrate domain-specific knowledge of PV mechanisms into the modeling process. Third, the generalization capability of few-shot learning needs to be improved. Variations in temperature and irradiance cause deformations in the I-V curves, even for the same type of PV system. Consequently, models trained on limited PV data exhibit poor generalization performance under diverse and complex operating conditions. Fourth, most existing cloud-edge collaboration methods indiscriminately upload all real-time data for inference. However, most of the samples are in the normal state and subject to frequent inference, resulting in additional communication and computation costs.

To address these challenges, a novel small-sample fault diagnosis framework is specifically designed for early-stage PV stations. The proposed framework is distinguished by its tightly coupled integration of three core components: the self-correcting model, few-shot learning Siamese network (SN), and cloud-edge collaboration, each synergistically enhancing the diagnostic accuracy, generalization capability, and resource efficiency of the system. A key innovation of our approach is the self-correcting model incorporated with PV mechanism knowledge. It transforms raw samples into defined standard states to enrich the representational capacity of the limited training data, enabling the model to generalize more effectively across complex and diverse operating conditions. Furthermore, considering the generalization capability of traditional contrastive learning methods is inherently affected by the distribution of the training set, the designed CNN-based SN is integrated with the self-correcting model to ensure that the network operates on standardized inputs. This process effectively mitigates the significant degradation of model performance across diverse operating conditions. Moreover, the self-correcting model provides reliable inputs for edge-side filtering, which eliminates misjudgments and missed detections. It allows the framework to transmit only fault samples to the cloud for detailed diagnosis, while normal samples are processed locally at the edge. As a result, the proposed method reduces communication and computational costs without compromising diagnostic precision, marking a substantial improvement over traditional approaches.

Our major contributions are summarized as follows.

1) A cloud-edge-based self-correcting-guided generalized contrastive learning framework is developed. To the authors' knowledge, it is the first successful attempt to extend the generalization of few-shot learning models to arbitrary temperature and irradiance conditions with high accuracy in PV fault diagnosis.

2) Based on the prior mechanistic knowledge of I-V curves, an end-to-end condition self-correcting model is constructed and integrated with the CNN-based SN. The range of applicable working conditions of the small-sample PV diagnostic model is significantly enlarged.

3) A type screening method based on similarity metrics is proposed from the perspectives of sample mean, variance, and covariance, which can quickly assess the optimal type for sample expansion, saving sample collection costs, while ensuring accuracy.

4) Considering interpretability, a fast fault filtering mechanism is further designed based on the defined similarity metrics to accurately identify fault samples and upload them to the cloud for further inference, which significantly saves computation and transmission costs.

The rest of this article is organized as follows. Section II reviews the related work. Section III introduces the system description. Section IV describes the proposed methods. Section V presents the simulation and experimental results. Finally, Section VI concludes this article.

II. RELATED WORK

Most recently, many contrastive learning-based fault diagnosis methods have emerged and achieved great success in several fields. Miao et al. [11] proposed a hierarchical contrastive learning method to obtain the characteristic representation of voltage ripple for dc/dc buck converter fault diagnosis. Qin et al. [12] proposed a forecasting-oriented contrastive learning method to predict the medium-term natural gas demand. Zhang et al. [13] integrated the multiscale attention mechanism and the multitarget contrastive learning method for rolling bearing fault diagnosis with limited labeled samples. Although the above-mentioned methods achieve small sample modeling, they fail to solve the problem of poor model generalization due to differences in the distribution of small training sets and varying working conditions of test data.

A promising way to enhance generalization is data augmentation through auxiliary information [14]. For PV fault diagnosis, the correction of I-V data has been proven to be effective. Ding et al. [15] proposed an optimal I-V correction method based on the mechanism model of PV cells. The feature enhancement was realized through I-V conversion, which effectively improved the accuracy of fault diagnosis. Wang et al. [16] introduced the uncertainty analysis method into the threshold design for identifying PV faults. By fitting the fault indicators, the generalization of the model was improved to a certain extent. However, most of the above methods are proposed based on specific topologies and cannot automatically adjust parameters in an end-to-end manner.

To balance real-time inference and complex model training, cloud-edge collaboration has been widely used in the fault diagnosis field. Liu et al. [17] proposed a graph adaptation framework based on cloud-edge orchestration to enhance the performance of the model under conditions of insufficient information. Xiang et al. [18] proposed a defect control framework
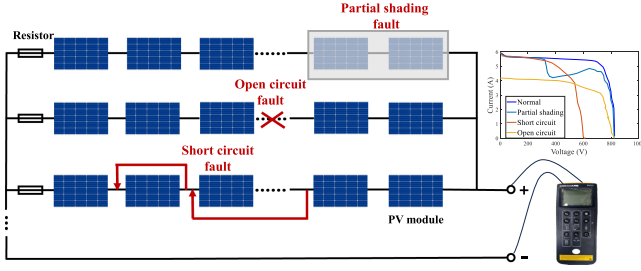
Fig. 1. Schematic diagram of PV array faults.

for hot-rolled coils, where the timeliness of control was ensured by reasonably allocating computing tasks between the cloud and edge computing layers. However, these methods lack edge-side data screening mechanisms for PV data.

III. SYSTEM DESCRIPTION

The PV array typically consists of several PV strings connected in parallel, where each string is composed of several PV modules connected in series. In this article, the normal state as well as three types of common faults are investigated, including partial shading, short circuit, and open circuit. Faults involving changes in the internal state of the PV module, such as degradation, hot spots, etc., as well as compound faults, are beyond the scope of this article.

Specifically, short-circuit faults are defined as the accidental connection between two points in the PV array. It manifests as an abnormally increased current. Open-circuit faults are typically caused by cable or connector disconnections that prevent a portion of the PV module or string from generating power. Partial shading faults occur when cloud cover, dust, or occlusions on the surface of PV modules reduce irradiance, leading to localized overheating and potentially causing hot spot effects under severe conditions.

I-V (current-voltage) curves reflect the electrical characteristics of PV systems, including key parameters, such as the maximum power point, open-circuit voltage, and short-circuit current. In this study, the original I-V curve is obtained by connecting the positive and negative terminals of the I-V tester to the output of the PV array, respectively. Starting from the open-circuit voltage (Voc), the I-V tester gradually reduces the voltage to 0, recording the corresponding current values throughout the process, as shown in Fig. 1.

IV. PROPOSED METHOD

A. Over View of the Framework

The architecture of the proposed self-correcting-guided generalized contrastive learning framework is shown in Fig. 2. It includes three parts: 1) Device side: PV Data collection. 2) Edge side: Data preprocessing, data correction, and sample filtering. 3) Cloud side: Training and inference of contrastive learning models.

During the inference phase, the data flow is as follows.

1) Step 1: PV data are initially captured by devices and undergoes preprocessing at the edge side. This step standardizes the dimensionality of the data for subsequent analysis.

2) Step 2: The raw data are then processed by the self-correcting model, which transforms it into defined standard operating conditions. This step ensures consistent and reliable input for subsequent analysis.

3) Step 3: The standardized samples are compared with normal samples under standard conditions using a fast fault filtering mechanism. This process identifies potential fault samples with high accuracy, leveraging the consistency provided by the self-correcting model.

4) Step 4: Only the identified potential fault samples are transmitted to the cloud, and are matched against the preconstructed support set with the trained contrastive learning model. This enables precise fault type identification and significantly reduces data transmission and computational overhead.

The unique strength of the proposed method lies in its seamless integration of the self-correcting model, contrastive learning, and the cloud-edge collaboration framework. The self-correcting model serves as the foundational pillar. On the one hand, this mechanism enables the SN with limited data to achieve high-precision fault diagnosis across diverse operating conditions. On the other hand, it guarantees the reliability of edge-side fault filtering, ensuring accurate and robust sample identification. This tightly coupled design not only addresses the limitations of traditional contrastive learning methods, but also enhances the cloud-edge collaboration framework, providing a transformative perspective to few-shot learning fault diagnosis. Details are described in the following.

B. Training of PV Condition Correction Models

1) Data Preprocessing: Original I-V data collected by PV devices cannot be directly used for model training due to varied data dimensions, uneven distribution of data points, and redundant information. To this end, we combine bilinear interpolation and resampling techniques to realize data preprocessing. Voltage points V_i and current points I_i are resampled equidistantly within the range of $[0, V_{oc}]$ and $[0, I_{sc}]$, where the V_{oc} and I_{sc} denote the value of open-circuit voltage and short-circuit current, respectively, $i = 1, 2, \ldots, 20$. The remaining values of current I_x and voltage V_x at 40 resampled points are calculated by the following:

$$I_x = \frac{(V_i - V_1) \cdot I_2 + (V_2 - V_i) \cdot I_1}{V_2 - V_1} \tag{1}$$

$$V_x = \frac{(I_i - I_1) \cdot V_2 + (I_2 - I_i) \cdot V_1}{I_2 - I_1} \tag{2}$$

where $[V_1, I_1]$ is the values of voltage and current at the left data point closest to the resampling point from the original I-V curve. Similarly, $[V_2, I_2]$ denotes the right side.

2) Construction of the Dataset: After that, the temperature, irradiance, and I-V vector are reconstructed to get a $40 \times$ 4-D array called the normal array. The four columns represent voltage, current, temperature, and irradiance, denoted as V, I, T, and G. It is worth noting that the proposed corrective method
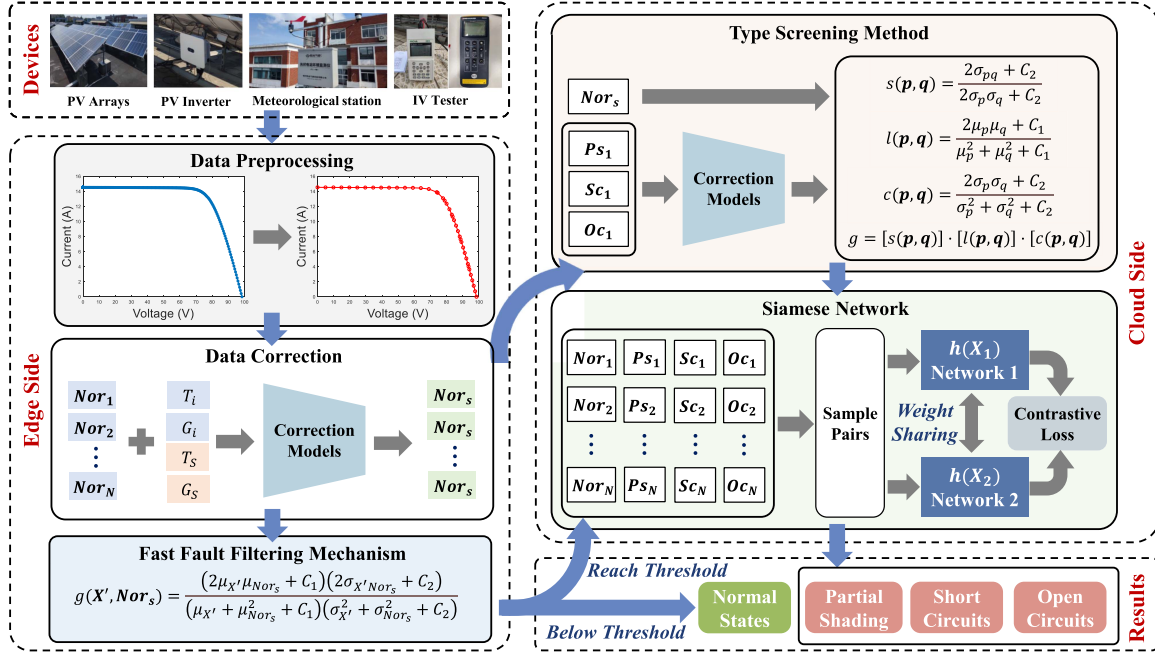
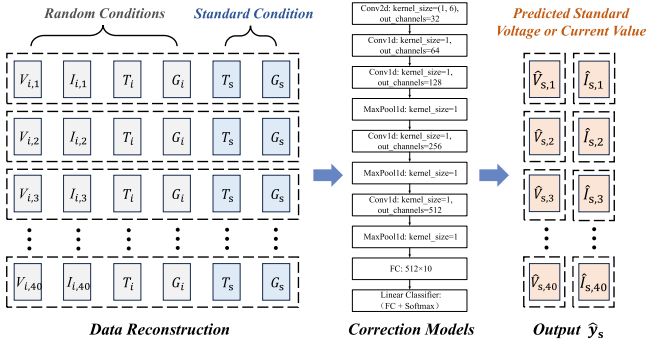Fig. 2. Architecture of the proposed self-correcting-guided generalized contrastive learning framework.

Fig. 3. Training process of PV condition correction models.

is implemented for each point, not the whole normal array. We define that $\boldsymbol{Nor_{i,j}}$ denotes the jth row vector of the ith normal array, $i = 1, 2, \ldots, N$, $j = 1, 2, \ldots, 40$. Thus, the total number of samples used to construct the dataset is $40 \times N$. Specifically, the normal array of the specified standard condition is defined as $\boldsymbol{Nor_s}$, $s \in [1, 2, \ldots, N]$. Data reconstruction is accomplished by inserting the specified standard condition temperature and irradiance into each row of the normal array, as shown in Fig. 3. Each sample $\boldsymbol{Nor_{i,j}}$ is constructed as a 1×7 vector, represented as

$$\begin{aligned} \boldsymbol{Nor_{i,j}} &= [V_{i,j}, I_{i,j}, T_i, G_i, T_s, G_s, L] \\ L_1 &= I_{s,j}, \dot{L}_2 = V_{s,j} \end{aligned} \quad (3)$$

where V_{ij} and $I_{i,j}$ denote the voltage and current value of the ith normal array in jth row, respectively. T_i and G_i denote the temperature and irradiance value of the ith normal array, respectively. T_s and G_s denote the temperature and irradiance

value of the standard normal array, respectively. L denotes the target value after correction, i.e., the label of supervised learning. As for current correction, we have $L = L_1$, while for voltage it is $L = L_2$.

3) Correction Models: IEC60891-2021-10 provides several typical mechanistic expressions to evaluate the effect of temperature and irradiance on the I-V curve. However, these methods are too ideal and may lead to large deviations when the measured irradiance differs by more than 40% from the irradiance at the temperature coefficient. Furthermore, some of the critical parameters are practically difficult to obtain. According to IEC60891-2021-10, a data-driven end-to-end condition correction model is proposed based on a CNN, as shown in Fig. 3. The dimensions of the model input $\boldsymbol{x}$ are six, corresponding to the first six columns of each sample $Nor_{i,j}$, that is, $\boldsymbol{x_{i,j}} = [V_{i,j}, I_{i,j}, T_i, G_i, T_s, G_s]$. The dimension of the model output $\hat{y}_{s,j}$ is one, which represents the corrected current or voltage value of the sample. For current correction, we have target $y_{s,j} = I_{s,j}$, while for voltage it is $y_{s,j} = V_{s,j}$. Since it is a regression problem, the mean square error (MSE) loss function is chosen. Although the current and voltage corrections are trained separately to enhance model accuracy, the two CNNs share the same structure

$$\text{loss} = \frac{1}{40N} \sum_{i=1}^{i=N} \sum_{j=1}^{j=40} (y_{s,j} - \hat{y}_{s,j})^2. \quad (4)$$

It is worth noting that the output of the self-correction model is the current and voltage vectors of the sample after condition transformation. By further incorporating the temperature and irradiance vectors under the specified standard condition, these vectors are reconstructed into standardized samples with

a dimensionality of 40×4. These transformed samples are then used as inputs for the fast fault filtering mechanism, type screening method, and inference process of the contrastive learning model. As for the training process of the contrastive learning model, the preprocessed is used directly with a dimensionality of 40×4. At this stage, omitting sample correction allows the model to fully leverage the richness and diversity of the limited training samples, significantly enhancing its ability to distinguish between different fault types.

C. Training of Contrastive Learning Models

1) Small-Sample Type Screening Method: It is worth noting that contrastive learning models are trained by comparing the similarity of discrete sample pairs. Inspired by the literature [19], we define three similarity assessment metrics based on the mean, standard deviation, and covariance of PV sample pairs for screening the type for modeling to reduce the cost of sample collection.

Specifically, for any two I-V vectors p and q to be compared, the mean comparison function is defined as

$$\mu_p = \frac{1}{N}\sum_{i=1}^{N} p_i, \mu_q = \frac{1}{N}\sum_{i=1}^{N} q_i \tag{5}$$

$$m(\boldsymbol{p}, \boldsymbol{q}) = \frac{2\mu_p\mu_q + C_1}{\mu_p^2 + \mu_q^2 + C_1} \tag{6}$$

where $\boldsymbol{p}_i$ and $\boldsymbol{q}_i$ represent the ith element in the I-V vector p and q, respectively. C_1 is a predefined constant. Similarly, the standard deviation comparison function is defined as

$$\sigma_p = \left(\frac{1}{N-1}\sum_{i=1}^{N}(p_i - \mu_p)^2\right)^{\frac{1}{2}} \tag{7}$$

$$\sigma_q = \left(\frac{1}{N-1}\sum_{i=1}^{N}(x_i - \mu_q)^2\right)^{\frac{1}{2}} \tag{8}$$

$$s(\boldsymbol{p}, \boldsymbol{q}) = \frac{2\sigma_p\sigma_q + C_2}{\sigma_p^2 + \sigma_q^2 + C_2} \tag{9}$$

where C_2 is a predefined constant.

The covariance comparison function is defined as

$$\sigma_{pq} = \frac{1}{N-1}\sum_{i=1}^{N}(p_i - \mu_p)(q_i - \mu_q) \tag{10}$$

$$c(\boldsymbol{p}, \boldsymbol{q}) = \frac{2\sigma_{pq} + C_2}{2\sigma_p\sigma_q + C_2}. \tag{11}$$

By combining the three functions, the final similarity comparison function g can be obtained

$$g(\boldsymbol{p}, \boldsymbol{q}) = [m(\boldsymbol{p}, \boldsymbol{q})] \cdot [s(\boldsymbol{p}, \boldsymbol{q})] \cdot [c(\boldsymbol{p}, \boldsymbol{q})]. \tag{12}$$

In the proposed method, the initial single samples of three types of faults are first corrected to the specified standard states. Afterward, the similarity is calculated with the normal sample in the standard state respectively. Existing studies have shown that enhancing the dissimilarity between sample pairs improves
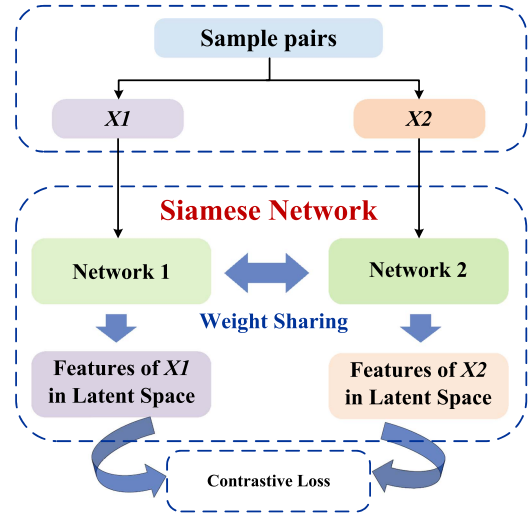

Fig. 4. Training process of SN models.

the model's ability to capture and distinguish variations among different samples. Considering these factors, the type with the least similarity is considered the optimal choice. The set of samples of this type is defined as $\boldsymbol{Fau}, |\boldsymbol{Fau}| = N_{op}$.

2) Construction of the Dataset: Since $N_{op} \ll N_{nor}$, we first downsample the normal samples to get $N_{op} = N'_{nor} = N_c$. Next, we define the sets of normal samples and fault samples as $\boldsymbol{J_1}$ and $\boldsymbol{J_2}$, respectively

$$\begin{aligned} \boldsymbol{J_1} &= \{\boldsymbol{Nor_i}\}, i = 1, 2, \ldots, N_c \\ \boldsymbol{J_2} &= \{\boldsymbol{Fau_i}\}, i = 1, 2, \ldots, N_c. \end{aligned} \tag{13}$$

Then, two samples from $\boldsymbol{J_1}$ or $\boldsymbol{J_2}$ are selected to construct the set $\boldsymbol{T_1}$ of same-type sample pairs, and $|\boldsymbol{T_1}| = 2C_{N_c}^2$.

$$\begin{aligned} \boldsymbol{T_1} &= \{\boldsymbol{Nor_i}, \boldsymbol{Nor_j}\} \cup \{\boldsymbol{Fau_i}, \boldsymbol{Fau_j}\} \\ & i, j = 1, 2, \ldots, N_c, i \neq j. \end{aligned} \tag{14}$$

Next, we select one sample from $\boldsymbol{J_1}$ and $\boldsymbol{J_2}$, respectively, to construct the set $\boldsymbol{T_2}$ of different-type sample pairs, and $|\boldsymbol{T_2}| = N_c{}^2$

$$\boldsymbol{T_2} = \{\boldsymbol{Nor_i}, \boldsymbol{Fau_j}\}, i, j = 1, 2, \ldots, N_c,. \tag{15}$$

Finally, we obtain the training dataset $\boldsymbol{T}$ for SN

$$\boldsymbol{T} = \boldsymbol{T_1} \cup \boldsymbol{T_2}. \tag{16}$$

In addition, an additional support set $\boldsymbol{S}$ needs to be constructed to cooperate with the test data for fault diagnosis

$$\boldsymbol{S} = \{\boldsymbol{Ps_s}, \boldsymbol{Sc_s}, \boldsymbol{Oc_s}\} \tag{17}$$

where $\boldsymbol{Ps_s}$, $\boldsymbol{Sc_s}$, and $\boldsymbol{Oc_s}$ denote samples of partial shading, short-circuit, and open-circuit faults under standard conditions.

3) Construction of Siamese Networks: In this article, the sub-networks are built based on two CNNs with the same structure and network weight, as shown in Fig. 4. The detailed structure of network 1 and network 2 is shown in Table I.

TABLE I
CONFIGURATION FOR THE SUB-NETWORKS

Layer	Output dimension	Detailed architecture of CNN
2-D CNN	$37 \times 1 \times 1$	$k = 44, C_{out} = 1, ss = 1, p = 0$
Squeeze	37×1	Dimension squeeze
1-D CNN	18×3	$k = 3, C_{out} = 3, ss = 2, p = 0$
1-D CNN	18×5	$k = 3, C_{out} = 5, ss = 1, p = 1$
MaxPool 1-D	8×5	$k = 4, ss = 2$
1-D CNN	8×8	$k = 3, C_{out} = 8, ss = 1, p = 1$
MaxPool 1-D	4×8	$k = 2, ss = 2$
1-D CNN	4×16	$k = 3, C_{out} = 16, ss = 1, p = 1$
MaxPool 1-D	1×16	$k = 4, ss = 1$
FC	16×10	Fully-connected Layer
Linear Classifier	10×4	FC + Softmax

The contrastive loss is chosen as the loss function for network training. For any input sample pair $\{\boldsymbol{X_1}, \boldsymbol{X_2}, Y\}$, we have

$$D_{\boldsymbol{W}}\left(h(\boldsymbol{X_1}), h(\boldsymbol{X_2})\right) = \| h(\boldsymbol{X_1}) - h(\boldsymbol{X_2})\|^2 \qquad (18)$$

$$Ls = (1 - Y)\frac{1}{2}(D_{\boldsymbol{W}})^2 + (Y)\frac{1}{2}\left\{\max(0, m - D_{\boldsymbol{W}})\right\}^2 \quad (19)$$

$$Y = \begin{cases} 1, \{\boldsymbol{X_1}, \boldsymbol{X_2}\} \in \boldsymbol{T_1} \\ 0, \{\boldsymbol{X_1}, \boldsymbol{X_2}\} \in \boldsymbol{T_2} \end{cases} \qquad (20)$$

where $m > 0$ is a boundary value. Different-type sample pairs only contribute to the loss function when the corresponding Euclidean distance is within this boundary. $\boldsymbol{W}$ is the network weight. Y is the label of the sample pair $(\boldsymbol{X_1}, \boldsymbol{X_2})$. $h(\cdot)$ represents the mapping function of the CNN sub-networks. $D_{\boldsymbol{W}}$ is the Euclidean distance between $\boldsymbol{X_1}$ and $\boldsymbol{X_2}$ in the latent variable space.

D. Cloud-Edge-Based Fast PV Fault Diagnosis

1) Edge-Side Fast Fault Filtering Mechanism: After data preprocessing and condition correction, the rapid fault filtering mechanism operates on the principle that both the sample $\boldsymbol{X'}$ to be detected and the standard normal sample $\boldsymbol{Nor_s}$ are under the same operating condition. If $\boldsymbol{X'}$ is in a normal state, its similarity to the normal sample will be extremely high. Conversely, if $\boldsymbol{X'}$ is a fault sample, its similarity will be significantly lower due to distortions caused by faults.

According to the type screening method above, the similarity assessment metrics based on the mean, standard deviation, and covariance are further calculated. Specifically, the mean comparison value is

$$m(\boldsymbol{X'}, \boldsymbol{Nor_s}) = \frac{2\mu_{\boldsymbol{X'}}\mu_{\boldsymbol{Nor_s}} + C_1}{\mu_{\boldsymbol{X'}}^2 + \mu_{\boldsymbol{Nor_s}}^2 + C_1}. \qquad (21)$$

The standard deviation comparison value is

$$s(\boldsymbol{X'}, \boldsymbol{Nor_s}) = \frac{2\sigma_{\boldsymbol{X'}}\sigma_{\boldsymbol{Nor_s}} + C_2}{\sigma_{\boldsymbol{X'}}^2 + \sigma_{\boldsymbol{Nor_s}}^2 + C_2}. \qquad (22)$$

The covariance comparison value is defined as

$$c(\boldsymbol{X'}, \boldsymbol{Nor_s}) = \frac{2\sigma_{\boldsymbol{X'}\boldsymbol{Nor_s}} + C_2}{2\sigma_{\boldsymbol{X'}}\sigma_{\boldsymbol{Nor_s}} + C_2}. \qquad (23)$$

By multiplying the three similarity metrics, we obtain a comprehensive similarity score M that robustly quantifies the alignment between $\boldsymbol{X'}$ and $\boldsymbol{Nor_s}$

$$M = \frac{(2\mu_{\boldsymbol{X'}}\mu_{Nor_s} + C_1)(2\sigma_{\boldsymbol{X'}Nor_s} + C_2)}{(\mu_{\boldsymbol{X'}}^2 + \mu_{Nor_s}^2 + C_1)(\sigma_{\boldsymbol{X'}}^2 + \sigma_{Nor_s}^2 + C_2)}. \qquad (24)$$

Then, we set a similarity threshold τ to evaluate whether the sample belongs to the normal state

$$\text{State} = g(\boldsymbol{X'}, \boldsymbol{Nor_s}) = \begin{bmatrix} 1, M < \tau \\ 0, M \geq \tau \end{bmatrix} \qquad (25)$$

where the value 1 indicates a fault and 0 indicates normal states. When the similarity falls below the threshold τ, the corresponding samples are uploaded to the cloud for further diagnosis and storage.

2) Cloud-Side Fault Classification: Once a fault sample is uploaded, the trained SN model is executed in the cloud. It calculates the similarity metric between the uploaded sample and each sample in the support set. Then, the fault type with the highest similarity is selected as the final diagnosis result. Finally, based on the cloud alarm information, the operator handles the faults on the PV device side, and the system returns to normal states. Thus, efficient and intelligent cloud-edge-based operation and maintenance of the PV system is realized through human-in-the-loop.

V. SIMULATION AND EXPERIMENT RESULTS

The effectiveness of the proposed PV fault diagnosis method is verified using simulated and actual collected data of normal states, partial shading faults, short-circuit faults, and open-circuit faults. For presentation clarity, they are abbreviated as 'Nor', 'Ps', 'Sc', and 'Oc', respectively. Details of the experiments conducted are described in the following.

A. Datasrts Description

1) Simulation Datasets: Simulink model is built to collect the simulation data. The simulation arrays consist of three PV strings connected in parallel, each containing six PV modules. To make it clear, each substring is further divided into two parts containing two and four series-connected PV modules, respectively. Specifically, partial shading faults are simulated by setting the shading gain below 1.0. Short-circuit faults are simulated by setting the short-circuit resistance to 0.001 Ω. Open-circuit faults are simulated by setting the open-circuit resistance to 1000 Ω. The temperature of the simulation data varies from 10 °C to 70 °C in steps of 2 °C. The irradiance ranges from 50 W m^{-2} to 1000 W m^{-2} with a step of 10 W m^{-2}. Each type contains 2976 samples, with a total sample size of 11 904. For training of correction models, we use 80% of normal data for training. The standard condition used as the correction target is set to 26 °C and 500 W m^{-2}. As for the training of the SN, sample pairs are constructed with 100 normal samples and 100 samples of the screened fault type to form the training set. Besides, the sample size of the test set is 11 704.

2) Actual Datasets: As shown in Fig. 5, the real data are collected from PV arrays with a capacity of 15 kW. It consists
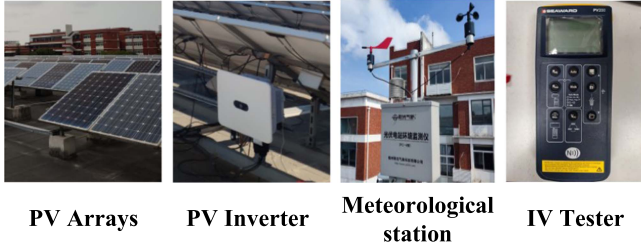
PV Arrays   **PV Inverter**   **Meteorological station**   **IV Tester**

Fig. 5. Actual PV arrays and devices for data collection.
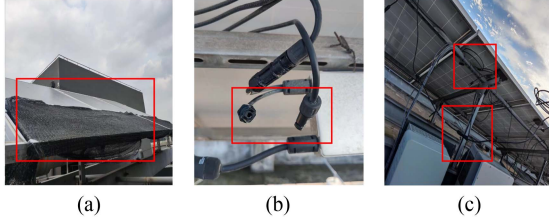

(a)   (b)   (c)

Fig. 6. Fault simulation in actual PV array. (a) Shading. (b) Short-circuit. (c) Open-circuit.

of two PV strings connected in parallel with each containing 22 PV panels connected in series. Specifically, short-circuit faults are simulated by reducing the number of panel connections in the string, partial shading faults by covering part of the PV panels with a curtain, and open-circuit faults by disconnecting part of the PV panels in the string, as shown in Fig. 6. Constrained by environmental factors and collection costs, we have tried to collect 100 real I-V curves of each type, with a total sample size of 400. The temperature varies from $32\,^{\circ}\text{C}$ to $48\,^{\circ}\text{C}$ and the irradiance ranges from $252\,\text{W}\,\text{m}^{-2}$ to $746\,\text{W}\,\text{m}^{-2}$. To train the correction model, we divide the training set and test set according to a ratio of 8:2. The standard condition used as the correction target is set to $40.5\,^{\circ}\text{C}$ and $500\,\text{W}\,\text{m}^{-2}$. To train the SN, the initial three fault types are set to have only one fault sample. Sample pairs are constructed with 80 normal samples and another 80 ones of the screened fault type to form the training set. In addition, the total number of samples in the test set is 240.

B. Implementation Details

A physical cloud-edge platform is built to validate the proposed method. A Raspberry Pi is regarded as the device side, whose role is to send pre-stored test data to the edge side. An NVIDIA Jetson NX development board is used as the edge side to carry out the data preprocessing, data correction, and fast fault filtering. The cloud side is chosen as HP ZBook Create G7 with Intel Core i9-10885H CPU, 32 GB RAM, and NVIDIA GeForce RTX 2070 Max-Q. This process simulates the handling of uploaded data from the edge side. Actually, the cloud-edge collaboration framework is currently the mainstream of practical operation and maintenance of PV stations, and the existing hardware configuration far exceeds the requirements mentioned above. Therefore, the proposed method will not be constrained by hardware limitations during deployment and is completely acceptable for practical applications.

TABLE II
RMSE OF CORRECTION MODEL IN SIMULATIONS

	Type of test samples				Average
	Normal	Shading	Short-circuit	Open-circuit	
RMSE	0.2393	0.2478	0.2507	0.2444	0.24555

TABLE III
SIMILARITY CALCULATION IN SIMULATIONS

	Types of faults			Screened type
	$g(Nor_s, Ps_s)$	$g(Nor_s, Sc_s)$	$g(Nor_s, Oc_s)$	
Similarity	0.78185	0.94419	0.93229	Partial shading

During the modeling process, the threshold τ for fault filtering is set to 0.95. The constants C_1 and C_2 are set to 6.5025 and 58.5225 based on reference [19]. The number of training epochs is set to 300. Since condition correction modeling is a regression problem, the root mean square error (RMSE) is chosen to verify the proposed method. For the fault classification problem, the accuracy, macroprecision, macro-recall, and macro-F1-score are selected as metrics to comprehensively evaluate the effectiveness of the proposed method. For ease of expression, the four indicators are abbreviated as 'Acc', 'mP', 'mR', and 'mF'.

C. Simulation Results

1) Correction Model Assessment: To validate the correction model, the RMSE for each type of correction model on the simulated test set is listed in Table II. It can be observed that the proposed condition correction models perform well for all four types studied with low RMSE values, even though these models are trained utilizing only normal state samples. It is worth noting that the correction model is a key part, and its validity directly affects the accuracy and generalization of our fault diagnosis method.

2) Comparison With Other Methods: In the simulation experiments, the three fault types are set to have only one fault sample initially. These three samples Ps_0, Sc_0, and Oc_0 are randomly selected from the simulation data of the corresponding type. They are first corrected to the specified standard condition based on the correction model. After that, based on the proposed small-sample type screening method, the similarity between the corrected three samples Ps_s, Sc_s, and Oc_s and the normal samples under the same condition Nor_s is calculated, as shown in Table III. It can be observed that the fault type with the lowest similarity is the Ps, so the SN is built based on this type and normal samples.

To verify the effectiveness of the proposed method, we compare the built model with several mainstream fault diagnosis methods in the PV field, including ELM [2], the residual network for multilabel learning (ML-SResNet) [20], and deep CNN [1]. The SN based on the contrastive learning method is chosen as the baseline [21]. These three methods involve multilabel learning, single-label learning, and contrastive learning, respectively. The results of the evaluation metrics are listed in Table IV.

TABLE IV
EVALUATION METRICS FOR DIFFERENT METHODS IN SIMULATIONS

	Test samples	Evaluation metrics			
		Acc	mP	mR	mF
ELM [2]	11 704	0.4307	0.2252	0.4331	0.2963
ML-SResNet [19]	11 704	0.2814	0.2151	0.2775	0.2423
SN [20]	11 704	0.3128	0.3952	0.3051	0.3444
CNN [1]	11 704	0.4267	0.2159	0.4267	0.2835
Proposed method	11 704	0.9820	0.9820	0.9820	0.9820

TABLE V
RMSE OF CORRECTION MODEL IN EXPERIMENTS

	Types of test samples				Average
	Normal	Shading	Short-circuit	Open-circuit	
RMSE	0.1617	0.1709	0.1816	0.1637	0.169475

TABLE VI
SIMILARITY CALCULATION IN EXPERIMENTS

	Types of faults			Screened type
	$g(Nor_s, Ps_s)$	$g(Nor_s, Sc_s)$	$g(Nor_s, Oc_s)$	
Similarity	0.73956	0.84986	0.81989	Partial Shading

TABLE VII
EVALUATION METRICS FOR DIFFERENT METHODS IN EXPERIMENTS

	Test samples	Evaluation metrics			
		Acc	mP	mR	mF
ELM [2]	240	0.1667	0.08334	0.5000	0.1429
ML-SResNet [19]	240	0.2308	0.1552	0.5000	0.369
SN [20]	240	0.6625	0.6510	0.6127	0.6313
CNN [1]	240	0.1667	0.1124	0.5000	0.1763
Proposed method	240	0.9958	0.9881	0.9881	0.9881
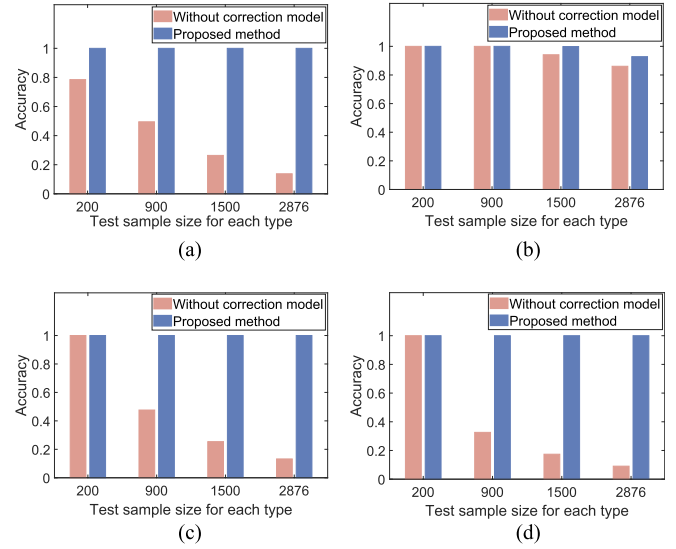
Fig. 7.   Accuracy and generalization of the SN. (a) Normal. (b) Partial shading. (c) Short circuit. (d) Open circuit.

The traditional methods based on the ELM, ML-SResNet, and CNN can no longer be used. In addition, the failure of the SN further suggests that it is almost impossible to build models with strong generalization only relying on existing SNs. In contrast, the proposed method can overcome the above problems and significantly improve the accuracy and generalization of the model. Specifically, the Acc, mP, mR, and mF have improved by about 55.13%, 58.68%, 54.89%, 98.2%, and 63.76%, respectively.

D. Experiment Results

1) Correction Model Assessment: To verify the effectiveness of the correction models on real data, the RMSE on the real test set is listed in Table V. It is clear that the proposed correction model achieves low RMSE values for all types.

First, the similarity of the single sample corrected for each fault type is calculated with the normal sample under the specified standard condition, respectively. Detailed results are listed in Table VI. It can be seen that the fault type with the lowest similarity is still the 'Ps', which is consistent with the conclusion in the previous simulation experiments.

2) Comparison With Other Methods: We have also conducted additional experiments based on real data to investigate the validity of the proposed method. Detailed evaluation metrics are listed in Table VII.

It can be seen that the SN method outperforms CNN, ELM, and ResNet methods in all the metrics and has a large improvement compared to the simulation experiments. Nevertheless, the metrics of the SN method are still very terrible and unable to meet the requirements of practical applications. Compared to the values of the optimal evaluation metrics in the compared

methods, the proposed method improves the Acc by 33.33%, mP by 33.71%, mR by 37.54%, and mF by 35.68%.

E. Ablation Experiments and Discussions

1) Assessment of the Self-Correcting Scheme: To validate the proposed self-correcting scheme, the accuracy and generalization of models are evaluated. As demonstrated by simulation data, with the number of test samples (indicating the complexity of environmental conditions) increasing, the model accuracy of four types declines in the absence of the correcting scheme. In contrast, the models that incorporated the scheme consistently maintain high accuracy, as shown in Fig. 7.

Due to the limited size of the actual data test set, all the test data are directly used for comparison, as shown in Fig. 8. Models with the proposed scheme achieve higher accuracy than those without the scheme for all four types.

2) Assessment of the Filtering Mechanism: To avoid misjudgments and omissions, determining the threshold is of critical importance. The threshold $\tau = 0.95$ is determined through a comprehensive evaluation of the results derived from the real and simulation training set. To validate the effectiveness of the threshold, tests on the entire test dataset are conducted, as listed in Table VIII. The normal and fault states can be accurately distinguished since the self-correction mechanism constrains
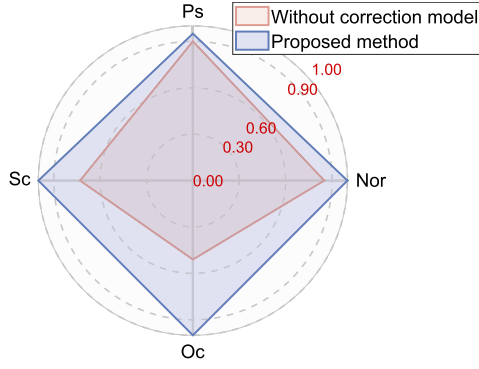
This article has been accepted for inclusion in a future issue of this journal. Content is final as presented, with the exception of pagination.

LIU et al.: SELF-CORRECTING-GUIDED GENERALIZED CONTRASTIVE LEARNING FRAMEWORK　　　　　9

Fig. 8.　Accuracy of each type compared by radar chart.

TABLE VIII
SAMPLE FILTERING DETAILS OF THE PROPOSED MECHANISM

Type	Threshold	Simulation data		Real data	
		min	max	min	max
Nor	0.95	**0.9881**	**0.9992**	**0.9872**	**0.9925**
Ps	0.95	0.7752	0.7819	0.7163	0.7396
Sc	0.95	0.9253	0.9442	0.8371	0.8499
Oc	0.95	0.9174	0.9323	0.8012	0.8201

TABLE IX
COMPARISON OF DIFFERENT METHODS FOR SAMPLE FILTERING

	Test samples	Filtering accuracy		
		Ours	Ref. [21]	Ref. [22]
Simulation data	240	**1.0000**	0.6861	0.5971
Real data	11704	**1.0000**	0.8072	0.7249

TABLE X
EVALUATION OF THE FILTERING MECHANISM OVER ESTABLISHED
TECHNIQUES

	Simulation data		Real data	
	data_cost	time_cost (s)	data_cost	time_cost (s)
ELM [2]	24.57% ↓	7.79 ↓	8.33% ↓	0.05 ↓
ML-SResNet [19]	24.57% ↓	13.69 ↓	8.33% ↓	0.09 ↓
SN [20]	24.57% ↓	34.80 ↓	8.33% ↓	0.24 ↓
CNN [1]	24.57% ↓	3.95 ↓	8.33% ↓	0.03 ↓

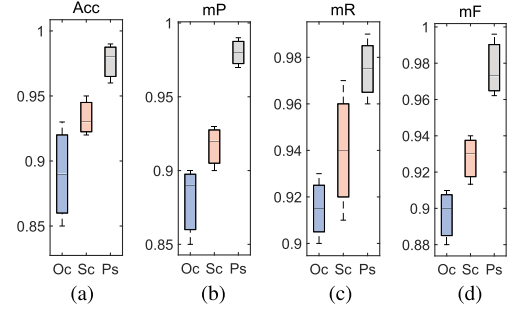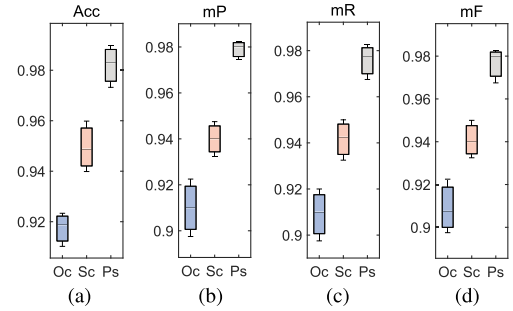Fig. 9.　Validation in simulations. (a) Acc. (b) mP. (c) mR. (d) mF.

Fig. 10.　Validation on real data. (a) Acc. (b) mP. (c) mR. (d) mF.

the fluctuation range of similarity values for samples of the same type, thereby ensuring the reliability and robustness of the filtering results.

Then, our mechanism is compared to the fault filtering methods proposed in [1] and [2], as shown in Table IX. The simulated data covers a much wider range of operating conditions compared to the collected real-world data. The compared methods perform better on real data than on simulated data, because they fail to generalize across a wider range of environmental conditions, such as temperature and irradiance fluctuations. In contrast, the proposed method ensures both accuracy and stability across diverse operating conditions by incorporating the self-correcting model.

In addition, the number of samples transferred to the cloud, and the total inference time are defined as 'data_cost' and 'time_cost', respectively. The advantages of this mechanism in reducing data transmission and computational cost over established techniques are listed in Table X. Since the proposed mechanism can filter out the normal samples in the test set, the data_cost is reduced by 24.57% and 8.33% on simulation and real data, respectively. Differences in reduced inference time result from the inherent inference speed of various methods.

3) Assessment of the Type Screening Method: The proposed type screening mechanism is validated by comparing the diagnostic accuracy for each of the selected fault types: short-circuit, open-circuit, and partial shading. The normal samples involved are ensured to be identical, and the results are shown in Figs. 9 and 10. It can be observed that the model built by selecting the partial shading type performs better compared to the other two types.

Then, the proposed method is compared with other small-sample type screening methods, including cosine similarity, Pearson correlation coefficient, RMSE, MTL [24], AL [25], and annotation check [3]. Tests are conducted on both simulated and real-world data across multiple data sizes, and the average type screening accuracy is depicted in Fig. 11. It is evident that the type screening accuracy of compared methods varies significantly with sample size. Although the accuracy of MTL and AL methods improves significantly as the sample size increases, this comes at the cost of higher initial dataset quality requirements. In contrast, the proposed
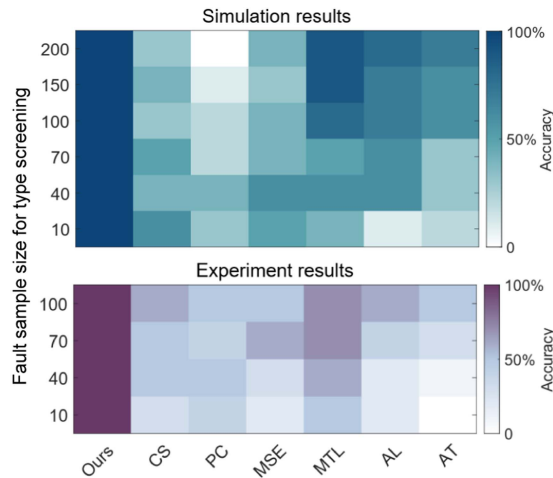
Fig. 11.   Comparison of different methods for type screening module across diverse data scenarios.
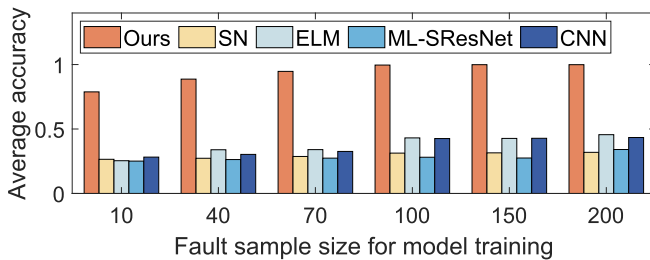

Fig. 12.   Average accuracy across diverse data scenarios.

method achieves 100% accuracy in identifying the optimal type across all scenarios, even with a small number of fault samples, because it effectively eliminates the impact of temperature and irradiance variations by seamlessly integrating the self-correcting model.

4) Assessment of Data Scenarios: To demonstrate the applicability of the proposed method to various sample sizes and operating conditions, the average diagnostic accuracy of the proposed method is tested based on simulation data in six different small sample situations, as shown in Fig. 12. The proposed method demonstrates significantly superior accuracy compared to other methods across all data conditions. As the number of fault samples increases, the accuracy of the proposed method gradually improves, achieving over 90% accuracy with only 70 samples and reaching 99.58% at a sample size of 100.

The average number of training epochs for ten independent experiments to converge to optimal accuracy are 140, 170, 230, 260, 260, and 280, respectively, which satisfy the setting of epochs of 300 in Section V-B.

VI. Conclusion

In this article, a cloud-edge-based self-correcting-guided generalized contrastive learning framework is proposed to enhance the accuracy and generalization capabilities for PV fault diagnosis in small-sample scenarios. Combining mechanistic knowledge, end-to-end condition correction models are constructed

to overcome the effects of varied temperature and irradiance on I-V curves. The range of applicable working conditions of the small-sample PV diagnostic model is significantly improved. In addition, a type screening method is proposed to maximize model accuracy, while saving sample collection costs. Furthermore, a fast fault filtering mechanism is proposed to reduce the computation and transmission costs. The proposed method has excellent accuracy and generalization and applies to real PV stations in small-sample scenarios with complex working conditions. The simulation and real data results show that the proposed method has excellent accuracy and generalization for partial shading, short-circuit, and open-circuit faults across a wide range of temperatures from $10\,°C$ to $70\,°C$ and irradiance from $50W\,m^{-2}$ to $1000W\,m^{-2}$, which covers the vast majority of real-world operating conditions. Currently, the initial training still requires relatively sufficient normal state samples and a small number of fault samples. How to extend the proposed method to more fault types, compound faults, zero-shot fault diagnosis, data privacy security, exceptionally extreme environmental conditions, and hardware deployment needs to be further investigated.

References

[1] Q. Liu, B. Yang, Y. Liu, K. Ma, and X. Guan, "Collaborate global and local: An efficient PV compound fault diagnosis scheme with multilabel learning and model fusion," *IEEE Trans. Instrum. Meas.*, vol. 72, 2023, Art. no. 2522816.

[2] Z. Chen et al., "Rapid and accurate modeling of PV modules based on extreme learning machine and large datasets of I-V curves," *Appl. Energy*, vol. 292, 2021, Art. no. 116929.

[3] B. Yang, Y. Lei, X. Li, N. Li, and A. K. Nandi, "Label recovery and trajectory designable network for transfer fault diagnosis of machines with incorrect annotation," *IEEE/CAA J. Automatica Sinica*, vol. 11, no. 4, pp. 932–945, Apr. 2024.

[4] U. Kumar et al., "An IoT and Semi-Supervised Learning-Based Sensorless Technique for Panel Level Solar Photovoltaic Array Fault Diagnosis," *IEEE Trans. Instrum. Meas.*, vol. 72, pp. 1–12, 2023, doi: 10.1109/TIM.2023.3287247.

[5] H. Wang, J. Wang, Y. Zhao, Q. Liu, M. Liu, and W. Shen, "Few-shot learning for fault diagnosis with a dual graph neural network," *IEEE Trans. Ind. Inform.*, vol. 19, no. 2, pp. 1559–1568, Feb. 2023.

[6] Z. Jia, Y. Fan, J. Zhang, C. Wei, R. Yan, and X. Wu, "Improving next location recommendation services with spatial-temporal multigroup contrastive learning," *IEEE Trans. Serv. Comput.*, vol. 16, no. 5, pp. 3467–3478, Sep./Oct. 2023.

[7] C. Li, X. Lei, Y. Huang, F. Nazeer, J. Long, and Z. Yang, "Incrementally contrastive learning of homologous and interclass features for the fault diagnosis of rolling element bearings," *IEEE Trans. Ind. Inform.*, vol. 19, no. 11, pp. 11182–11191, Nov. 2023.

[8] J. Ji, H. Jia, Y. Ren, and M. Lei, "Supervised contrastive learning with structure inference for graph classification," *IEEE Trans. Netw. Sci. Eng.*, vol. 10, no. 3, pp. 1684–1695, May/Jun. 2023.

[9] Y. Yu, L. Guo, H. Gao, Y. He, Z. You, and A. Duan, "FedCAE: A new federated learning framework for edge-cloud collaboration based machine fault diagnosis," *IEEE Trans. Ind. Electron.*, vol. 71, no. 4, pp. 4108–4119, Apr. 2024.

[10] B. Li and Y. Yang, "Distributed fault detection for large-scale systems: A subspace-aided data-driven scheme with cloud-edge-end collaboration," *IEEE Trans. Ind. Inform.*, vol. 20, no. 10, pp. 12200–12209, Oct. 2024.

[11] J. Miao, Y. Liu, Q. Yin, B. Ju, G. Zhang, and H. Wang, "A novel soft fault detection and diagnosis method for a DC/DC buck converter based on contrastive learning," *IEEE Trans. Power Electron.*, vol. 39, no. 1, pp. 1501–1513, Jan. 2023.

[12] D. Qin, G. Liu, Z. Li, W. Guan, S. Zhao, and Y. Wang, "Federated deep contrastive learning for mid-term natural gas demand forecasting," *Appl. Energy*, vol. 347, 2023, Art. no. 121503.

[13] W. Zhang, D. Chen, Y. Xiao, and H. Yin, "Semi-supervised contrast learning based on multiscale attention and multitarget contrast learning for bearing fault diagnosis," *IEEE Trans. Ind. Inform.*, vol. 19, no. 10, pp. 10056–10068, Oct. 2023.

[14] Y. Zhuo and Z. Ge, "Auxiliary information-guided industrial data augmentation for any-shot fault learning and diagnosis," *IEEE Trans. Ind. Inform.*, vol. 17, no. 11, pp. 7535–7545, Nov. 2021.

[15] K. Ding et al., 'Feature extraction and fault diagnosis of photovoltaic array based on current–voltage conversion," *Appl. Energy*, vol. 353, 2024, Art. no. 122135.

[16] H. Wang, J. Zhao, Q. Sun, and H. Zhu, "Probability modeling for PV array output interval and its application in fault diagnosis," *Energy*, vol. 189, 2019, Art. no. 116248.

[17] B. Liu and C.-H. Chen, "An adaptive multihop branch ensemble-based graph adaptation framework with edge-cloud orchestration for condition monitoring," *IEEE Trans. Ind. Inform.*, vol. 19, no. 10, pp. 10102–10113, Oct. 2023.

[18] F. Xiang, S. Zhou, Y. Zuo, and F. Tao, "Digital twin driven end-face defect control method for hot-rolled coil with cloud-edge collaboration," *IEEE Trans. Ind. Inform.*, vol. 19, no. 2, pp. 1674–1682, Feb. 2023.

[19] Z. Wang, A. Bovik, H. Sheikh, and E. Simoncelli, "Image quality assessment: From error visibility to structural similarity," *IEEE Trans. Image Process.*, vol. 13, no. 4, pp. 600–612, Apr. 2004.

[20] Z. He, P. Chu, C. Li, K. Zhang, H. Wei, and Y. Hu, "Compound fault diagnosis for photovoltaic arrays based on multi-label learning considering multiple faults coupling," *Energy Convers. Manage.*, vol. 279, 2023, Art. no. 116742.

[21] F. Koochaki and L. Najafizadeh, "A siamese convolutional neural network for identifying mild traumatic brain injury and predicting recovery," *IEEE Trans. Neural Syst. Rehabil. Eng.*, vol. 32, pp. 1779–1786, 2024.

[22] W. Cao, J. Zeng, and Q. Liu, "FLCL: Feature-level contrastive learning for few-shot image classification," *IEEE Trans. Emerg. Topics Comput.*, to be published, doi: 10.1109/TETC.2025.3546366.

[23] Y. Zhang, Q. Cui, L. Shi, and J. Li, "Privacy-preserving incipient fault identification in distribution networks under small sample and imbalanced data distribution conditions," *IEEE Trans. Ind. Inform.*, vol. 20, no. 11, pp. 12848–12859, Nov. 2024.

[24] X. Dong, T. Ouyang, S. Liao, B. Du, and L. Shao, "Pseudo-labeling based practical semi-supervised meta-training for few-shot learning," *IEEE Trans. Image Process.*, vol. 33, pp. 5663–5675, 2024.

[25] Z. Yan et al., "Contrastive open-set active learning-based sample selection for image classification," *IEEE Trans. Image Process.*, vol. 33, pp. 5525–5537, 2024.

Qi Liu received the B.Eng. degree in automation from the College of Information Science and Engineering, Northeastern University, Shenyang, China, in 2019, and the Ph.D. degree in control science and engineering from Shanghai Jiao Tong University, Shanghai, China, in 2024.

He is currently a Research Associate with the Department of Automation, Shanghai Jiao Tong University, Shanghai. His current research interests include machine learning, fault diagnosis, intelligent operation and maintenance of photovoltaic system, and multienergy optimization management.

Bo Yang (Senior Member, IEEE) received the Ph.D. degree in electrical engineering from the City University of Hong Kong, Hong Kong, in 2009.

He is currently a Distinguished Professor with Shanghai Jiao Tong University, Shanghai, China. He has been the Principal Investigator in several research projects, including the NSFC Key Project and National Science Fund for Distinguished Young Scholars. His research interests include optimization and control for energy networks and Internet of Things.

Dr. Yang was the recipient of the Young Scientist Award of Chinese Association of Automation. He is on the steering committee of Asian Control Association. He is currently an Associate Editor for IEEE TRANSACTIONS ON NETWORK SCIENCE AND ENGINEERING.

Mingxuan Cai received the B.Eng. degree in automation from Xi'an Jiaotong University, Xi'an, China, in 2022. He is currently working toward the Ph.D. degree n control science and engineering with the Department of Automation, Shanghai Jiao Tong University, Shanghai, China.

His research interests include data-driven and electrochemical mechanism modeling, health prognosis, and optimal control of flow battery system.
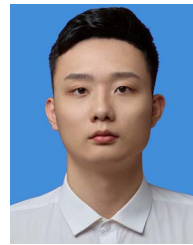
Yuxiang Liu received the B.Eng. degree in automation and the Ph.D. degree in control science and engineering from Shanghai Jiao Tong University, Shanghai, China, in 2020 and 2025, respectively, all in control science and engineering.

He is currently a Postdoctoral Researcher with the Department of Automation, Shanghai Jiao Tong University. His current research interests include microservice deployment and intelligent manufacturing.

Kai Ma (Senior Member, IEEE) received the B.Eng. degree in automation and the Ph.D. degree in control science and engineering from Yanshan University, Qinhuangdao, China, in 2005 and 2011, respectively.

He is currently an Associate Professor with the Department of Automation, School of Electrical Engineering, Yanshan University. In 2011, he joined Yanshan University. From 2013 to 2014, he was a Postdoctoral Research Fellow with Nanyang Technological University, Singapore. His current research interests include demand response in smart grid and resource allocation in communication networks.

Xinping Guan (Fellow, IEEE) received the B.Sc. degree in mathematics from Harbin Normal University, Harbin, China, in 1986, and the Ph.D. degree in control science and engineering from the Harbin Institute of Technology, Harbin, in 1999.

He is currently the Chair Professor with Shanghai Jiao Tong University, Shanghai, China, where he is the Director of the Key Laboratory of Systems Control and Information Processing, Ministry of Education of China. Before that, he was the Executive Director of Office of Research Management, Shanghai Jiao Tong University, a Full Professor, and Dean of Electrical Engineering, Yanshan University, Qinhuangdao, China. As a Principal Investigator, he has finished/been working on more than 20 national key projects. He is the Leader of the prestigious Innovative Research Team of the National Natural Science Foundation of China. He is an Executive Committee Member of Chinese Automation Association Council and the Chinese Artificial Intelligence Association Council. He has authored or coauthored five research monographs, more than 200 papers in IEEE transactions and other peer-reviewed journals, and numerous conference papers. His current research interests include industrial network systems, smart manufacturing, and underwater networks.

Dr. Guan was the recipient of the Second Prize of the National Natural Science Award of China in both 2008 and 2018, the First Prize of Natural Science Award from the Ministry of Education of China in both 2006 and 2016, the IEEE Transactions on Fuzzy Systems Outstanding Paper Award in 2008. He is a National Outstanding Youth honored by NSF of China, and Changjiang Scholar's by the Ministry of Education of China and State-Level Scholar of New Century Bai Qianwan Talent Program of China.